Small polarons and point defects in barium cerate

Michael Swift,[1] Anderson Janotti,[2,*] and Chris G. Van de Walle[2]

[1]*Department of Physics, University of California, Santa Barbara, California 93106-9530, USA*
[2]*Materials Department, University of California, Santa Barbara, California 93106-5050, USA*
(Received 17 July 2015; published 28 December 2015)

Barium cerate ($BaCeO_3$) is a well-known ionic conductor of both hydrogen and oxygen. In applications, it is frequently doped (for instance with Y) to increase stability and promote diffusion. However, the effects of doping and native defects are not fully understood. Computational studies have been stymied by the nature of the conduction band, which is made up of cerium $4f$ states. These states present a challenge to *ab initio* techniques based on density functional theory within the standard approximations for exchange and correlation. Using a hybrid functional, we investigate the effects of hydrogen impurities and native defects on the electrical and optical properties of $BaCeO_3$. We discuss the tendency of excess electrons or holes to localize in the form of small polarons. We also explore the interactions of polarons with hydrogen impurities and oxygen vacancies, and their impact on luminescence properties.

I. INTRODUCTION

Hydrogen is known to readily incorporate in many oxides with the perovskite crystal structure, such as barium cerate [1] [Fig. 1(a)]. $BaCeO_3$ has been explored for use in numerous applications, including steam electrolysis for hydrogen production, hydrogen gas sensors, hydrogen pumps and membranes, and solid oxide fuel cells for operation at intermediate temperatures [2]. Historically, *ab initio* techniques based on density functional theory (DFT) have encountered obstacles when applied to cerium-containing compounds. This is due in large part to the important role cerium $4f$ electrons play in the physics of these materials. Localization and correlation effects are strong for bands of f electrons, and exchange-correlation functionals such as the local density approximation (LDA) or generalized gradient approximation (GGA) fall short in capturing the physics of f states. Hybrid functionals, on the other hand, combine exact Hartree-Fock exchange with GGA, and have been shown to improve the description of strongly localized carriers [3–6]. They have also proven accurate in the description of defects in a wide variety of semiconductor systems, correcting the band-gap problem of LDA and GGA [7]. These advantages make DFT with hybrid functionals very well suited for the study of barium cerate.

Hydrogen incorporation into $BaCeO_3$ often proceeds through the reaction [2]

$$H_2O + V_O^{2+} \leftrightarrow O_O + 2H_i^+ \tag{1}$$
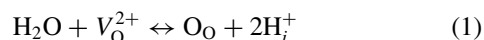
where V_O^{2+} indicates an oxygen vacancy acting as a double donor, O_O indicates an occupied oxygen site, and H_i^+ indicates a proton occupying an interstitial position in the lattice. A thorough understanding of ionic conduction in barium cerate thus requires an investigation of interstitial hydrogen and oxygen vacancies, as well as of their interaction, including the possible formation of a defect complex.

$BaCeO_3$ is often doped with elements such as yttrium ($BaCe_{1-x}Y_xO_3$) or neodymium ($BaCe_{1-x}Nd_xO_3$). This process increases the chemical stability of the material and enhances oxygen vacancy concentrations, while still maintaining good ionic conduction. We therefore also investigate substitutional yttrium, Y_{Ce}, as well as its complexes. Since yttrium has one fewer valence electron than cerium, yttrium on the cerium site is expected to act as a single acceptor. In its negative charge state, it will strongly interact with positively charged defects such as interstitial hydrogen or oxygen vacancies.

In this paper we address charge localization (polaron formation), defects and impurities, and the behavior of hydrogen in $BaCeO_3$ using a hybrid density functional approach, which produces structural and electronic properties in good agreement with experiment. We find that localization of electrons in cerium $4f$ states plays an important role in the formation and charge compensation of native defects and hydrogen impurities. We calculate formation energies of defects and binding energies of defect complexes, which are essential for describing hydrogen motion through the material. Our results also allow us to interpret features that have been observed in luminescence experiments [9].

II. COMPUTATIONAL METHODOLOGY

Our calculations are based on DFT with a hybrid functional. They were performed with the projector augmented wave (PAW) method [10] as implemented in the Vienna Ab Initio Simulation Package (VASP) [11]. The chosen pseudopotential for cerium included 46 electrons in the core ([Kr] $4d^{10}$), leaving 12 valence electrons ($5s^2 5p^6 4f 5d 6s^2$) for the PAW calculation. Lattice parameters and band structure were calculated for a 20-atom conventional cell using a $4 \times 4 \times 4$ Monkhorst-Pack grid in reciprocal space [12]. Defect and polaron calculations were performed in a 160-atom supercell using a single point in reciprocal space, $k = (0.25,0.25,0.25)$. All calculations used a plane-wave energy cutoff of 400 eV. We verified precision by performing tests with 500-eV cutoffs and a $2 \times 2 \times 2$ k-point mesh. The tests gave discrepancies of less than 2% for formation energies, lattice parameters, and the band gap, indicating that our results are converged with respect to both k-point density and plane-wave cutoff.

---

*Present address: Department of Materials Science and Engineering, University of Delaware, Newark, Delaware 19716-3106, USA.
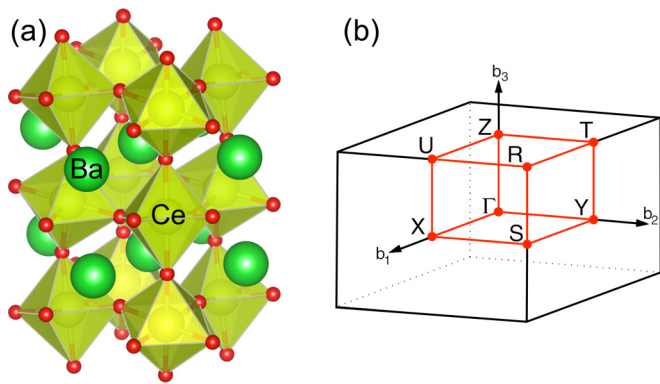
FIG. 1. (Color online) (a) Visualization of the orthorhombic perovskite structure of barium cerate. Cerium ions are octahedrally coordinated by oxygen, with barium ions interspersed. (Barium ions are green, cerium-centered octahedra are yellow, and oxygen ions are red.) (b) Brillouin zone of the orthorhombic lattice, illustrating the conventional path along high-symmetry directions [8].

The hybrid exchange-correlation functional of Heyd, Scuseria, and Ernzerhof [13] was employed with 25% mixing and screening parameter $\omega = 0.20\,\text{Å}^{-1}$. This combination of parameters is commonly referred to as HSE06 [14].

III. RESULTS

A. Structural parameters

The low-temperature phase of barium cerate is an orthorhombic perovskite with moderate octahedral tilting and very similar a and b lattice parameters [15]. Table I shows the structural parameters of pure $BaCeO_3$ as calculated using HSE, and Fig. 1 shows a visualization of the structure. The calculated structural parameters are in good agreement with experiment.

B. Band structure

Figure 2 shows the calculated band structure of barium cerate. The band gap of 4.17 eV is in very good agreement with the accepted experimental value of 4.1 eV obtained from optical absorption spectroscopy [17]. Since HSE has been shown to correctly describe the cerium-containing oxides CeO_2 and Ce_2O_3 [18,19], including the $4f$ conduction-band states, we expect $BaCeO_3$ to also be well described by HSE.

TABLE I. Structural parameters of $BaCeO_3$ as calculated using HSE, compared with experimental values [15]. The angles measure the degree of octahedral tilting: $\angle_1$ is the in-plane ($\perp z$) Ce-O-Ce angle for cerium atoms separated along the z direction, and $\angle_2$ is the out-of-plane ($\parallel z$) Ce-O-Ce angle.

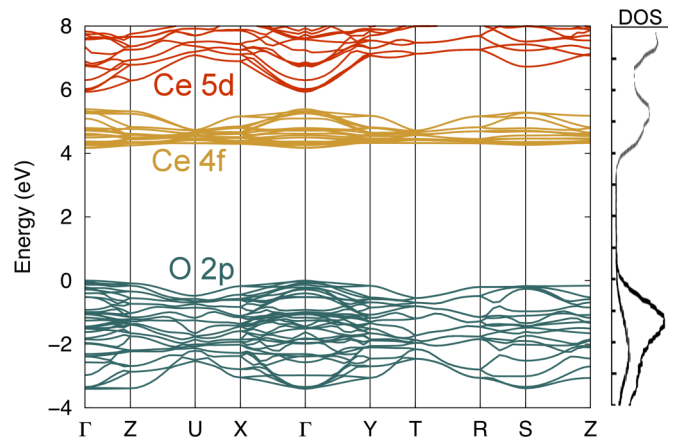|	Theory	Expt.
a (Å)	6.233	6.237
b (Å)	6.223	6.218
c (Å)	8.782	8.780
$\angle_1$	159.4°	158.8°
$\angle_2$	156.6°	156.1°

FIG. 2. (Color online) Band structure of $BaCeO_3$ as calculated with HSE, plotted along the high-symmetry lines illustrated in Fig. 1(b). The valence bands are primarily O $2p$ states. The band gap is 4.17 eV. The lowest conduction bands are composed of Ce $4f$ states; they are separated from the higher-lying Ce $5d$ states by a gap of 0.54 eV. The experimental density of states from Ref. [16] is plotted on the right-hand side for comparison.

The valence band is primarily composed of O $2p$ states, and is separated from the conduction band by a direct gap at Γ. There is a further gap of 0.54 eV between the Ce $4f$ and $5d$ bands.

HSE corrects the band-gap problem of the commonly used GGA of Perdew, Burke, and Ernzerhof (PBE) [20], which predicts a gap of 2.21 eV for $BaCeO_3$. HSE also reduces the width of the $4f$ band and narrows the gap between the $4f$ and $5d$ bands as compared to PBE results. This brings the band structure into good agreement with experimental density-of-states results [16], as shown in Fig. 2.

C. Formation energies

We analyze defect formation within the grand canonical ensemble. The formation energy of a defect X in charge state q is given by [21]

$$E^f[X^q] = E_{\text{tot}}[X^q] - E_{\text{tot}}[\text{bulk}] - \sum_i n_i \mu_i + q E_F + \Delta^q$$

(2)

where $E_{\text{tot}}[X^q]$ is the total energy of a supercell containing the defect X in charge state q, $E_{\text{tot}}[\text{bulk}]$ is the total energy of the supercell without the defect, n_i indicates the number of atoms of type i added ($n_i > 0$) or removed ($n_i < 0$) to form the defect, and μ_i are the corresponding chemical potentials of the species, discussed in more detail in the next paragraph. A defect in charge state q is formed by adding or removing electrons from the neutral state. The chemical potential of electrons in the solid is the Fermi energy E_F. By convention, $E_F = 0$ at the top of the valence band. Δ^q is a charge-state-dependent correction due to the finite size of the supercell, which was calculated using the method of Refs. [22,23]. We used an experimental value of 98 for the static dielectric constant, calculated from the capacitance measurements and experimental geometry of Ref. [24]. Due

to the high value of the dielectric constant, the magnitude of Δ^q is small (of the order of a few 0.01 eV and uniformly less than 0.07 eV).

The atomic chemical potentials μ_i are referenced to the total energies per atom of their respective ground-state phases. For μ_O, the reference is half of the total energy of an O_2 molecule. The chemical potentials are treated as variables that can depend on growth or processing conditions. However, bounds are placed on these values by imposing the conditions for stability of $BaCeO_3$ in thermodynamic equilibrium:

$$\mu_{Ba} + \mu_{Ce} + 3\mu_O = \Delta H_f(BaCeO_3), \qquad (3)$$

where $\Delta H_f(BaCeO_3)$ is the formation enthalpy of $BaCeO_3$. In order to prevent formation of bulk Ba and Ce phases, and to prevent loss of O_2, the chemical potentials are bounded from above by

$$\mu_{Ba}, \mu_{Ce}, \mu_O \leqslant 0. \qquad (4)$$

To prevent formation of secondary BaO, BaO_2, CeO_2, and Ce_2O_3 phases, it is also required that

$$\mu_{Ba} + \mu_O \leqslant \Delta H_f(BaO), \qquad (5)$$

$$\mu_{Ba} + 2\mu_O \leqslant \Delta H_f(BaO_2), \qquad (6)$$

$$\mu_{Ce} + 2\mu_O \leqslant \Delta H_f(CeO_2), \qquad (7)$$

$$2\mu_{Ce} + 3\mu_O \leqslant \Delta H_f(Ce_2O_3). \qquad (8)$$

The quantities $\Delta H_f(BaO)$, $\Delta H_f(BaO_2)$, $\Delta H_f(CeO_2)$, and $\Delta H_f(Ce_2O_3)$ are the enthalpies of formation of BaO, BaO_2, CeO_2, and Ce_2O_3, respectively, and these are calculated from first principles and listed in Table II. The inequalities above allow us to describe the region of chemical potentials in the $\mu_{Ce} - \mu_O$ plane for which $BaCeO_3$ is stable.

It is worth noting that PBE has been shown to outperform HSE in the calculation of the reduction energy of CeO_2 to Ce_2O_3 [19,25]. However, the HSE formation enthalpies themselves are closer to experiment; the PBE reduction energies are accurate due to a cancellation of errors in formation enthalpies for the particular case of ceria [19]. To allow comparison with other materials and to maintain consistency with the electronic structure calculations we have chosen to use HSE throughout this work.

Figure 3 shows the resulting phase diagram for the system. For a fixed μ_O, we observe that $BaCeO_3$ forms in a narrow

TABLE II. Calculated enthalpy of formation per formula unit of barium cerate and the possible limiting phases. Experimental values [26,27] are provided for comparison.

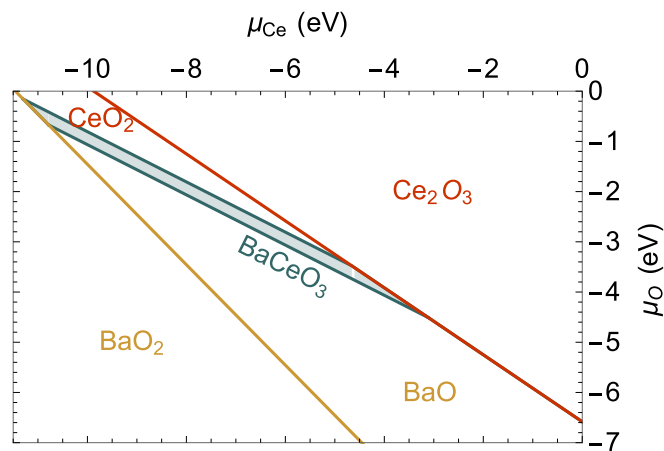| Compound	ΔH_f (eV)	
	Theory	Experiment
$BaCeO_3$	-17.23	-17.52
BaO	-5.10	-5.68
BaO_2	-5.77	-6.57
CeO_2	-11.61	-11.30
Ce_2O_3	-19.75	-18.65
H_2O	-2.67	-2.51
Y_2O_3	-19.18	-19.74

FIG. 3. (Color online) Phase diagram of $BaCeO_3$. The region of cerium and oxygen chemical potentials for which $BaCeO_3$ is stable is indicated by the (green) shaded region. Above this region, CeO_2 will form. Below this region, BaO or BaO_2 will form.

μ_{Ce} window of width 0.26 eV. For our calculations of defect formation energies, we fix μ_{Ce} as a function of μ_O by assuming the system lies on a line running through the middle of the $BaCeO_3$ region of stability (which is quite narrow). We can then choose μ_O to reflect different growth conditions. For impurities, we perform similar calculations to fix μ_H (limited by formation of H_2O) and μ_Y (limited by the formation of Y_2O_3). Thus the only remaining variable is μ_O. For the calculation of formation energies, we considered two values: $\mu_O = -0.42$ eV (near the oxygen rich limit) and $\mu_O = -2.5$ eV (relatively oxygen poor, corresponding to O_2 gas at 1100 K and 0.1 MPa [28]).

Following Eq. (2), we calculate the formation energy of various defects and defect complexes in all possible charge states. We plot the formation energies by finding the most stable charge state at each value of the Fermi level, and then plotting the energy of that charge state (Fig. 4). Note that using Y_2O_3 as the solubility-limiting phase for μ_Y leads to the lowest possible formation energy for Y_{Ce} defects before precipitation of Y_2O_3. Realistic μ_Y values will be lower, and formation energies will be correspondingly higher.

Figure 4 shows that the formation energy of Y_{Ce} is low, and hence the impurity will easily incorporate in the lattice, particularly under more oxygen-rich (cerium-poor) conditions. The incorporation of yttrium, which acts as an acceptor, will drive the Fermi level down, which in turn promotes the incorporation of point defects or impurities with donor character, such as oxygen vacancies or hydrogen. Charge neutrality between the positively charged donors and the negatively charged acceptors will then determine the position of the Fermi level. Hydrogen impurities have low formation energies, which enables high solubility and is conducive to good proton conduction.

When hydrogen and yttrium are simultaneously present, $Y_{Ce}^- + H_i^+$ complexes will easily form. This may impede proton diffusion. To assess the impact of these complexes, we calculate a binding energy of hydrogen to the yttrium impurity. The binding energy E_b between two entities A and B when they form a complex AB is defined by adding the formation
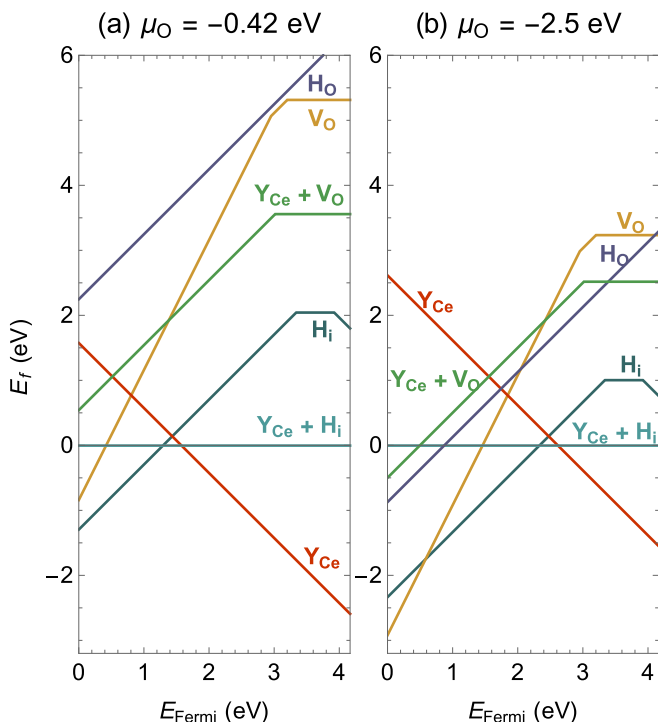
FIG. 4. (Color online) Calculated formation energies of various impurities, defects, and complexes as a function of Fermi level for given values of the oxygen chemical potential.

energies of the isolated species and subtracting the energy of the complex [29]:

$$E_b(AB) = E^f(A) + E^f(B) - E^f(AB). \qquad (9)$$

Calculated values are listed in Table III. While the binding energy between Y_{Ce}^- and H_i^+ is relatively modest (0.26 eV), it is sizable on the scale of the proton migration barrier in this material (0.22 to 0.58 eV) [30]. In equilibrium, at a given temperature, $Y_{Ce}^- - H_i^+$ complexes will only be present in concentrations larger than those of the isolated species if the binding energy of 0.26 eV exceeds the formation energies of the isolated species [31]; however, even if this criterion is not met, trapping of hydrogen at Y impurities may impact kinetics.

If yttrium forms a complex with an oxygen vacancy, the resulting entity is positively charged over a range of Fermi levels between 0 and almost 3 eV; such positive charged complexes would not trap protons, due to Coulomb repulsion. Formation of such complexes would therefore be desirable,

TABLE III. Calculated binding energies of defect complexes and between defects and polarons in barium cerate, as given by Eq. (9).

Complex	Binding energy (eV)
$Y_{Ce}^- + H_i^+$	0.26
$Y_{Ce}^- + V_O^{2+}$	0.19
$H_i^+ + e_{polaron}^-$	0.05
$V_O^{2+} + e_{polaron}^-$	0.44
$V_O^{2+} + 2\,e_{polaron}^-$	0.62
$Y_{Ce}^- + h_{polaron}^+$	0.22

but unfortunately the binding energy is quite small (0.19 eV, Table III) and hence they are unlikely to occur.

D. Polarons

We expect that localization of carriers will be important in barium cerate, due to the relatively flat dispersion of the bands. This localization manifests itself in the form of polarons: localized electrons together with a lattice distortion. In our calculations, we form an isolated polaron by introducing an extra electron into bulk BaCeO$_3$ and locally breaking the symmetry of the lattice through small perturbations of the atomic positions. This allows an electron to localize near the perturbation. The lattice is then allowed to relax, forming a polaron. The energy of this configuration is lower than that of an electron in the conduction-band minimum, and the energy difference is the self-trapping energy.

Our calculations show that polaron formation is extremely favorable for an electron in the conduction band [Fig. 5(a)]: the self-trapping energy is 780 meV. A hole polaron in the valence band has a smaller, but still significant, self-trapping energy of 150 meV. An electron polaron on a cerium atom stretches the Ce-O bond length by 2% and decreases Ce-O-Ce angles by 2%. This distortion is highly localized; the displacements from the nominal lattice sites are smaller than the calculational error bars already for cerium atoms directly adjacent to the polaron. This high degree of localization of the lattice distortion indicates that electrons in BaCeO$_3$ localize in the form of small polarons.

Polarons are likely to occur in the vicinity of defects that have a charge opposite to that of the carrier. This can be more energetically favorable than having electrons localize on the defect itself. The neutral charge state of interstitial hydrogen is an example. While H_i^- is a "genuine" defect state (the proton sits between two barium atoms and two electrons are localized on the defect center), we find that similar configurations with only one electron (H_i^0) are unstable. Instead, the proton tends to bond to an oxygen atom (as in H_i^+), while an electron polaron forms on an adjacent cerium atom [Fig. 5(b)]. This leads to an entity that is overall neutral, but it would be inaccurate to describe this as "neutral interstitial hydrogen" since the electron is not localized on the defect center.

The case of oxygen vacancies is similar: the $+1$ charge state consists of $V_O^{2+} + e_{polaron}^-$, and the neutral charge state consists of $V_O^{2+} + 2e_{polaron}^-$ [Fig. 5(c)]. While the structure of the polaron bound to H_i^+ is similar to that of an isolated polaron, polarons bound to the oxygen vacancy have a different magnetic quantum number. This state is likely favored because it allows higher electron density near the positively charged defect center. When two polarons are bound to the same vacancy, they have opposite spins due to the partial overlap of their wave functions at the defect center.

Binding energies of polarons to various donors in BaCeO$_3$ are listed in Table III. Note that when two polarons are bound to an oxygen vacancy the energy cost to remove one of the polarons is only 0.18 eV.

In order to study the hopping of polarons, we calculated the energies of a series of structures with atomic positions interpolating between polaron configurations on two adjacent sites. The highest energy among these structures has roughly
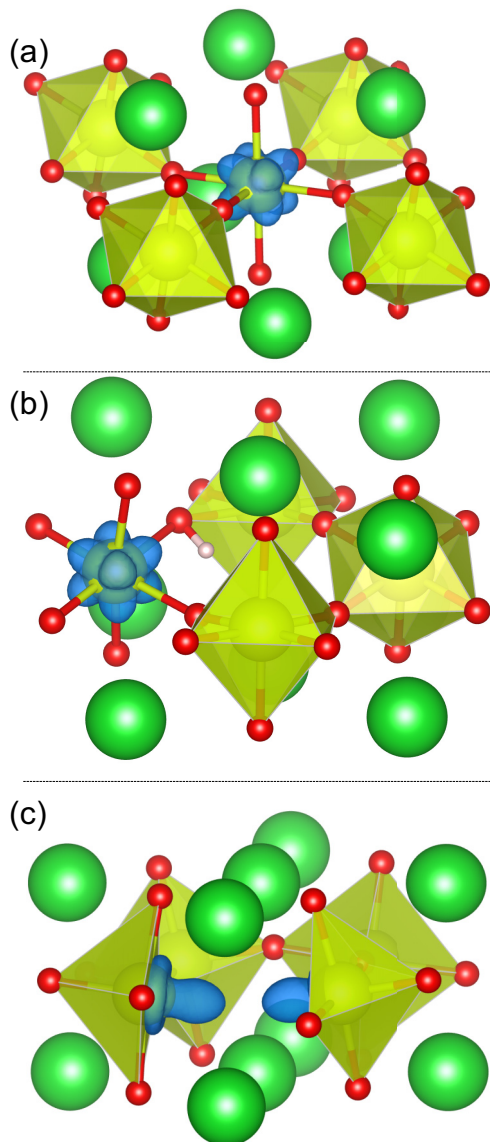
FIG. 5. (Color online) Visualization of the structure of electron polarons in various configurations: (a) e_{polaron}^- in bulk, (b) $H_i^+ + e_{\text{polaron}}^-$, and (c) $V_O^{2+} + 2e_{\text{polaron}}^-$. Color coding as in Fig. 1; the hydrogen ion is white. Charge-density isosurfaces at 10% of the maximum are also shown (in blue) for the polaron state.

half of the polaron localized on both sites. This was taken to be the transition state for hopping between the sites, and its energy (referenced to the relaxed polaron) is the activation energy for polaron hopping. This activation energy is 0.29 eV for in-plane hopping ($\perp$ c) and 0.31 eV for out-of-plane hopping ($\parallel$ c).

E. Optical properties

Our first-principles studies allow for the calculation of optical properties, including the energetics of radiative transitions [32]. We have applied this methodology to barium cerate. Our results for key processes are presented in Table IV, and two important cases are illustrated in Fig. 6. In these diagrams, the horizontal axis is a generalized "configuration coordinate": atomic configurations were generated by interpo-

TABLE IV. Calculated energy peaks of optical absorption and emission processes in barium cerate.

Ground state	Excited state	Absorption (eV)	Emission (eV)
H_i^+	$H_i^0 + h_{\text{VBM}}^+$	4.25	2.31
V_O^{2+}	$V_O^+ + h_{\text{VBM}}^+$	3.38	2.43
Bulk	$h_{\text{polaron}}^+ + e_{\text{CBM}}^-$	4.17	2.99
Bulk	$e_{\text{polaron}}^- + h_{\text{VBM}}^+$	4.17	2.43

lating the atomic positions between two structures. In Fig. 6(a) the first structure corresponds to the atomic configuration for the ground state of the oxygen vacancy in a 2+ charge state, and the second structure to the atomic configuration for the ground state of the oxygen vacancy in a + charge state. The generalized coordinate is thus representative of the displacements of atoms surrounding the oxygen vacancy as the charge
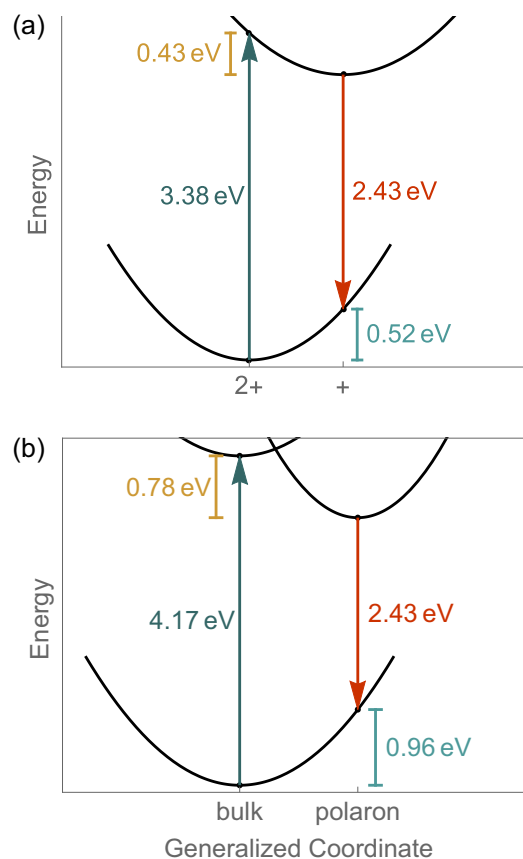

FIG. 6. (Color online) (a) Configuration coordinate diagram illustrating absorption and luminescence processes associated with oxygen vacancies. The lower parabola represents an oxygen vacancy in its 2+ charge state, while the upper parabola represents the 1+ charge state. We predict absorption peaked near 3.4 eV and luminescence peaked around 2.4 eV. (b) Configuration coordinate diagram showing band-to-band absorption, polaron formation, and luminescence due to radiative recombination of the polaron with a free hole. The lowest parabola represents the bulk, the highest parabola represents the bulk with an e^-, h^+ pair, and the intermediate parabola represents an electron polaron. We predict this process will also contribute to the luminescence peak near 2.4 eV.

state is changed. In Fig. 6(b) the first structure corresponds to the atomic positions in bulk $BaCeO_3$, and the second structure corresponds to the atomic configuration corresponding to an electron polaron. Here, the coordinate represents the relaxation of (mainly) oxygen atoms away from the localizing electron (cf. Sec. III D). For each intermediate configuration, the electronic structure was solved self-consistently. The upward-pointing arrow illustrates the formation of an electron-hole pair through absorption of a photon. Absorption is followed by lattice relaxation through phonon-mediated nonradiative processes. The downward-pointing arrow illustrates the luminescence step, in which the electron-hole pair recombines radiatively, emitting a photon. Finally, the lattice goes through another phonon-mediated relaxation into the ground-state configuration. A full description of these processes would involve transitions between vibronic states, and would allow the prediction of luminescence line shapes [32]. Here, we focus on the most probable radiative transitions, which are represented by the arrows in Fig. 6 and correspond to peaks in absorption or luminescence spectra; these peak energies are listed in Table IV.

Kompan *et al.* [9] reported luminescence spectra for $BaCeO_3$ prepared under various conditions. The authors observed luminescence peaks at 2.48 and 2.92 eV after subgap UV excitation. They suggested that this luminescence originated from the capture of an electron in the conduction band by a cerium atom to form Ce^{3+}, i.e., an electron polaron. The formation of a polaron from an electron in the conduction band involves an energy gain of 0.78 eV, a phonon-assisted process that is nonradiative. We therefore feel the luminescence mechanism proposed in Ref. [9] cannot be correct. Instead, we propose a process in which the incoming 3.68-eV photons in the experiment can excite $V_O^{2+} \rightarrow V_O^+ + h_{VBM}^+$. Our calculated 2.43-eV luminescence peak corresponding to $V_O^+ + h_{VBM}^+ \rightarrow V_O^{2+}$ is in very good agreement with the observed peak at 2.48 eV, and our 2.99-eV

peak for $h_{polaron}^+ + e_{CBM}^-$ is in very good agreement with the observed peak at 2.92 eV. Kompan *et al.* also reported that the luminescence signal disappears when the sample is prepared in an oxygen-rich environment, supporting our attribution of the signal to oxygen vacancies.

IV. CONCLUSIONS

We have investigated the structural and electronic properties of barium cerate, and shown that they are well described by DFT using a hybrid exchange-correlation functional. Formation, properties, and interactions were calculated for the impurities and intrinsic defects that are most relevant for proposed applications. We have found that polaron formation is an important phenomenon in the study of $BaCeO_3$, and it is essential to take the effects of polarons into account when describing the behavior of defects and impurities. These effects have been explored in detail, calculating formation energies, favorable charge states, polaron binding energies, and optical transition levels. We expect that, in the case of other cerium-containing oxides such as CeO_2 and $SrCeO_3$, the same general principles will hold.

[1] H. Iwahara, T. Esaka, H. Uchida, and N. Maeda, Solid State Ionics **3**, 359 (1981).

[2] D. Medvedev, A. Murashkina, E. Pikalova, A. Demin, A. Podias, and P. Tsiakaras, Prog. Mater. Sci. **60**, 72 (2013).

[3] B. G. Janesko, T. M. Henderson, and G. E. Scuseria, Phys. Chem. Chem. Phys. **11**, 443 (2009).

[4] A. Carvalho, A. Alkauskas, A. Pasquarello, A. K. Tagantsev, and N. Setter, Phys. Rev. B **80**, 195205 (2009).

[5] A. Janotti, C. Franchini, J. B. Varley, G. Kresse, and C. G. Van de Walle, Phys. Status Solidi Rapid Res. Lett. **7**, 199 (2013).

[6] A. Janotti, J. B. Varley, M. Choi, and C. G. Van de Walle, Phys. Rev. B **90**, 085202 (2014).

[7] T. M. Henderson, J. Paier, and G. E. Scuseria, Phys. Status Solidi B **248**, 767 (2011).

[8] W. Setyawan and S. Curtarolo, Comput. Mater. Sci. **49**, 299 (2010).

[9] M. Kompan, Y. Baikov, B.-T. Melekh, and A. Yakubovich, Phys. Solid State **44**, 1263 (2002).

[10] P. E. Blöchl, Phys. Rev. B **50**, 17953 (1994).

[11] G. Kresse and J. Furthmüller, Phys. Rev. B **54**, 11169 (1996).

[12] H. J. Monkhorst and J. D. Pack, Phys. Rev. B **13**, 5188 (1976).

[13] J. Heyd, G. E. Scuseria, and M. Ernzerhof, J. Chem. Phys. **118**, 8207 (2003).

[14] J. Paier, M. Marsman, K. Hummer, G. Kresse, I. C. Gerber, and J. G. Angyan, J. Chem. Phys. **125**, 249901 (2006).

[15] K. Takeuchi, C.-K. Loong, J. R. Jr., J. Guan, S. Dorris, and U. Balachandran, Solid State Ionics **138**, 63 (2000).

[16] T. Higuchi, H. Fukawa, and H. Takahashi, Trans. Mater. Res. Soc. Jpn. **36**, 15 (2011).

[17] T. He, P. Ehrhart, and P. Meuffels, J. Appl. Phys. **79**, 3219 (1996).

[18] P. J. Hay, R. L. Martin, J. Uddin, and G. E. Scuseria, J. Chem. Phys. **125**, 034712 (2006).

[19] J. L. F. Da Silva, M. V. Ganduglia-Pirovano, J. Sauer, V. Bayer, and G. Kresse, Phys. Rev. B **75**, 045121 (2007).

[20] J. P. Perdew, K. Burke, and M. Ernzerhof, Phys. Rev. Lett. **77**, 3865 (1996).

[21] C. Freysoldt, B. Grabowski, T. Hickel, J. Neugebauer, G. Kresse, A. Janotti, and C. G. Van de Walle, Rev. Mod. Phys. **86**, 253 (2014).

[22] C. Freysoldt, J. Neugebauer, and C. G. Van de Walle, Phys. Rev. Lett. **102**, 016402 (2009).

[23] C. Freysoldt, J. Neugebauer, and C. G. Van de Walle, Phys. Status Solidi B **248**, 1067 (2011).

[24] E. Mladenova, Z. Stoynov, and D. Vladikova, Impedance Contributions Online **12**, P9:1 (2014).

[25] J. Paier, C. Penschke, and J. Sauer, Chem. Rev. **113**, 3949 (2013).

[26] E. Cordfunke, A. Booij, and M. Huntelaar, J. Chem. Thermodyn. **30**, 437 (1998).

[27] Edited by W. Martienssen, O. Madelung, and K.-H. Hellwege, *Thermodynamic Properties of Inorganic Materials Pure Substances.*, Landolt-Bornstein - Group IV Physical Chemistry - Numerical Data and Functional Relationships in Science and Technology, Vol. 19A4, Part 4 (Springer, Berlin, 2001).

[28] M. W. Chase, *NIST-JANAF Thermochemical Tables*, J. Phys. and Chem. Ref. Dat. Mon. (AIP, New York, 1998).

[29] C. G. Van de Walle, Phys. Rev. B **56**, R10020 (1997).

[30] J. Hermet, M. Torrent, F. Bottin, G. Dezanneau, and G. Geneste, Phys. Rev. B **87**, 104303 (2013).

[31] C. G. Van de Walle and J. Neugebauer, J. Appl. Phys. **95**, 3851 (2004).

[32] A. Alkauskas, J. L. Lyons, D. Steiauf, and C. G. Van de Walle, Phys. Rev. Lett. **109**, 267401 (2012).